iScience

CellPress
OPEN ACCESS

Article

Post-surgical wireless monitoring of arterial health progression

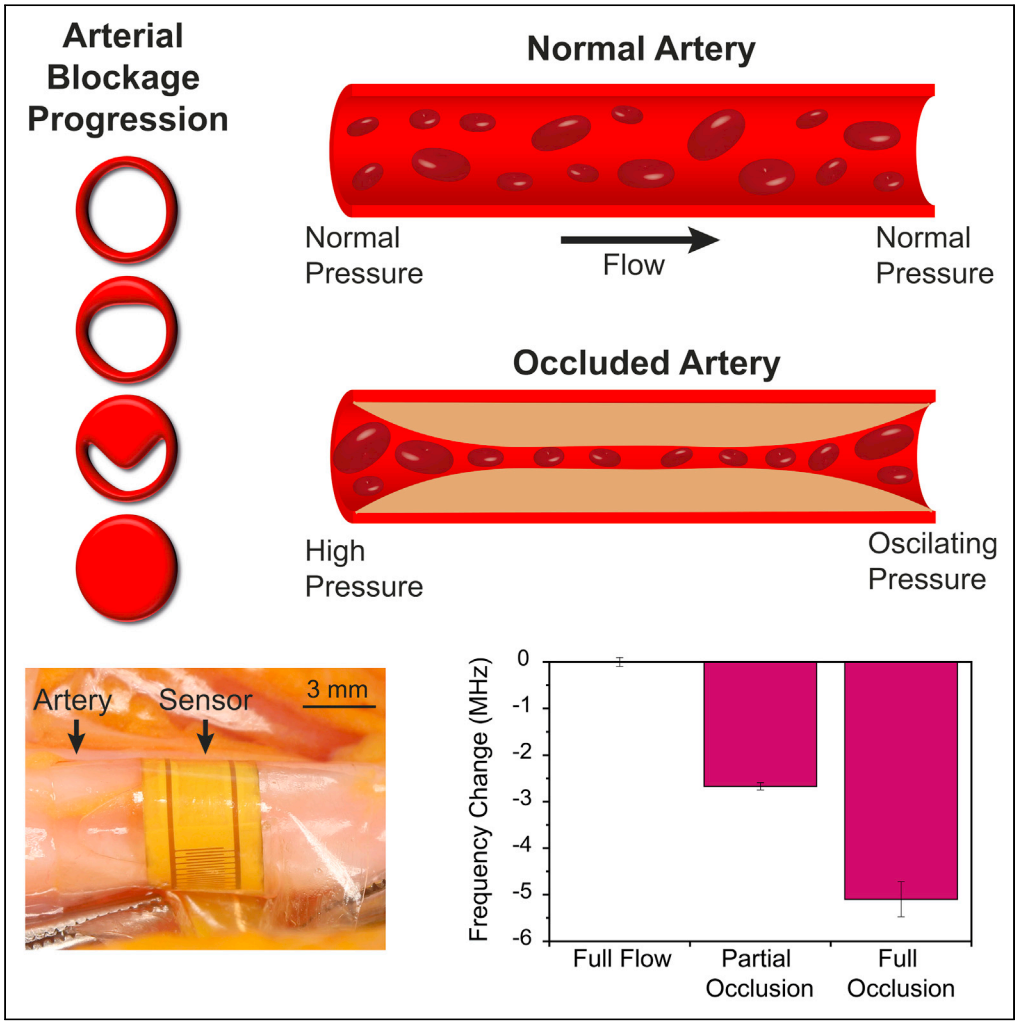

Sara R.A. Ruth, Min-gu Kim, Hiroki Oda, ..., James Chang, Paige M. Fox, Zhenan Bao

pfox@stanford.edu (P.M.F.)
zbao@stanford.edu (Z.B.)

Highlights

Novel wireless biocompatible, microstructured capacitive sensors

An implanted sensor enables early detection and prevention of diseases after surgery

The sensor effectively detects progression of an arterial blockage in various artery types

The sensor demonstrates capabilities in vitro, in vivo, and in a human cadaver

Ruth et al., iScience 24, 103079
September 24, 2021
https://doi.org/10.1016/j.isci.2021.103079

iScience

CellPress
OPEN ACCESS

Article

Post-surgical wireless monitoring of arterial health progression

Sara R.A. Ruth,[1] Min-gu Kim,[1,4] Hiroki Oda,[2,3] Zhen Wang,[2,3] Yasser Khan,[1] James Chang,[2,3] Paige M. Fox,[2,3,*] and Zhenan Bao[1,5,*]

SUMMARY

Early detection of limb ischemia, strokes, and heart attacks may be enabled via long-term monitoring of arterial health. Early stenosis, decreased blood flow, and clots are common after surgical vascular bypass or plaque removal from a diseased vessel and can lead to the above diseases. Continuous arterial monitoring for the early diagnosis of such complications is possible by implanting a sensor during surgery that is wirelessly monitored by patients after surgery. Here, we report the design of a wireless capacitive sensor wrapped around the artery during surgery for continuous post-operative monitoring of arterial health. The sensor responds to diverse artery sizes and extents of occlusion in vitro to at least 20 cm upstream and downstream of the sensor. It demonstrated strong capability to monitor progression of arterial occlusion in human cadaver and small animal models. This technology is promising for wireless monitoring of arterial health for pre-symptomatic disease detection and prevention.

INTRODUCTION

Continuous long-term arterial health monitoring is integral for early detection of peripheral vascular disease and stroke prevention. Elevated blood pressure was the leading cause of premature death worldwide in 2015 (Forouzanfar et al., 2017). Studies have shown that hypertension, high cholesterol, and atherosclerosis all cause differences in the blood flow rate, pattern, and pressure in the artery and are the main causes of peripheral vascular disease (PVD), heart attack, and stroke (Makin et al., 2001; Stroke, 2017; Virani et al., 2020). In 2015, PVD accounted for 20% of all hospital admissions in the United States, with incidence rates rising (Fanari and Weintraub, 2015). In fact, it is often overlooked in routine physical exams (Ouriel, 2001). Heart disease is the leading cause of death in the United States (Virani et al., 2020) while stroke accounts for 1 in 20 deaths and costs an estimated $34 billion in the United States each year (Stroke, 2017) and is the leading cause of serious long-term disability (Stroke, 2017).

Previously, we have reported sensors for arterial pulse wave monitoring on patients' wrists to obtain ambulatory blood pressure (Boutry et al., 2015). Moreover, we relied on external, indirect sensors—sensors not placed on the vessels themselves (Swartz et al., 1988)—to monitor vascular mechanical properties and function due to a lack of sensors with direct measurement capabilities (Vardoulis et al., 2016). A major limitation of these methods is that sensors are not directly implanted on the arteries, which limits the ability to monitor specific arteries, especially pertinent in high-risk areas such as surgical sites. However, recent work in our lab has shown that direct, continuous, in vivo measurement using an arterial-pulse sensor in animal models is possible (Boutry et al., 2019). Further, recent work has demonstrated that occlusion monitoring is possible ex vivo using an artificial artery (Li et al., 2020). Here, we aim to design a wireless pressure sensor that can detect changes in arterial pressure both in the short term and long term to allow continuous monitoring of vascular health and function post-surgery (Figure 1). The sensor is targeted for implantation during open surgeries such as carotid artery bypass, carotid endarterectomy, coronary artery bypass, and lower extremity bypass, among others. Short-term use would allow monitoring of the vascular anastomosis, where two vessels are connected in the aforementioned surgeries. This is a common site of early stenosis, decreased blood flow, and/or clot. Design and fabrication of a wireless sensor that can directly and continuously monitor local blood pressure long-term would allow for early detection and consequently more timely treatment to avoid heart attack, stroke, and limb ischemia depending on the surgical site. Heart attack prevention would be targeted for patients who undergo a coronary artery bypass surgery. Approximately, 8% of patients—over 32,000 patients—have a non-fatal heart attack within the first 5 years after the bypass surgery (Alexander and Smith, 2016; Lamy et al., 2016). In fact, hospital readmission following a coronary artery bypass costs

[1]Department of Chemical Engineering, Stanford University, Stanford, CA, USA

[2]Division of Plastic and Reconstructive Surgery, Stanford University School of Medicine, Stanford, CA, USA

[3]Division of Plastic Surgery, Veterans Affairs Palo Alto, Palo Alto, CA, USA

[4]Present address: Department of Information and Communication Engineering, Inha University, Incheon, South Korea

[5]Lead contact

*Correspondence: pfox@stanford.edu (P.M.F.), zbao@stanford.edu (Z.B.)

https://doi.org/10.1016/j.isci.2021.103079

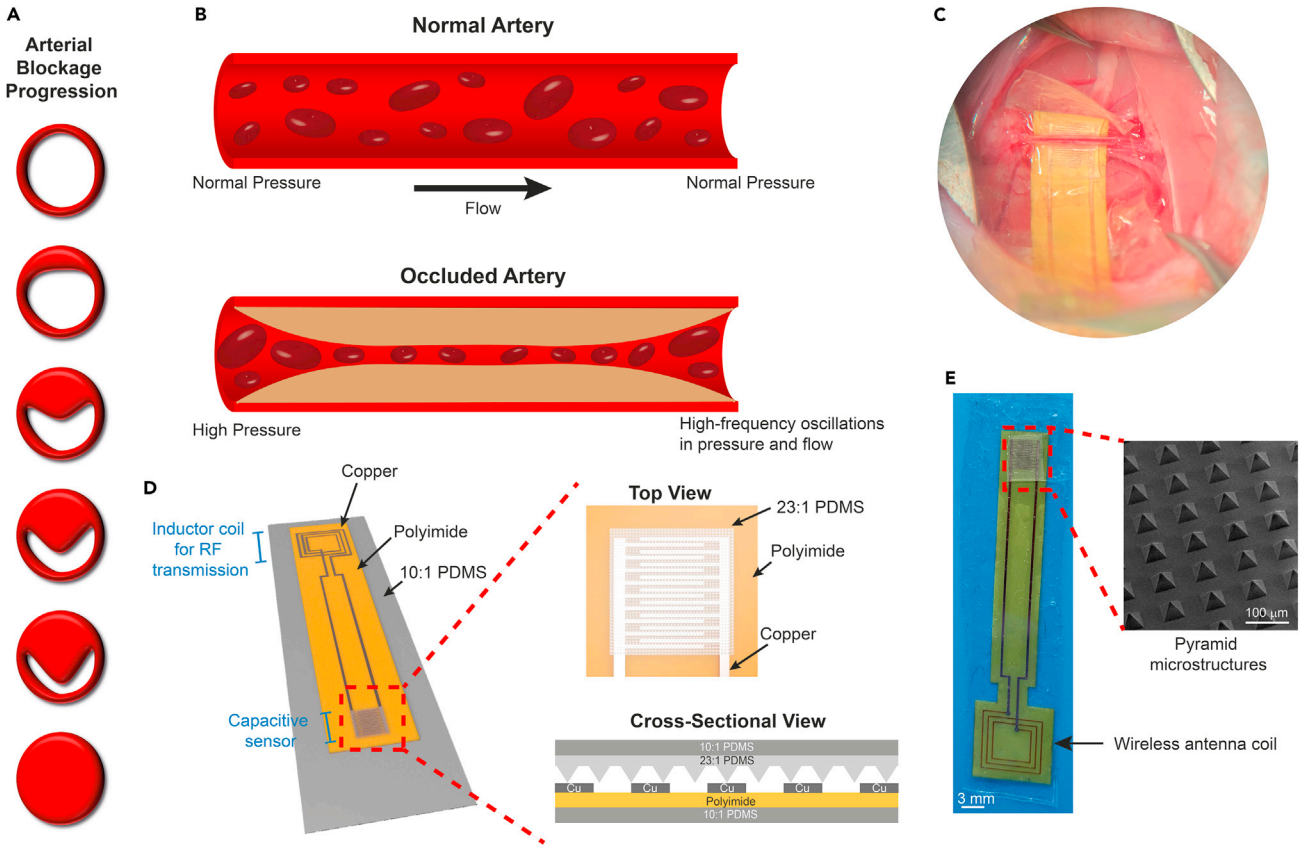

Figure 1. Biocompatible, flexible arterial-pressure sensor design

(A) Early detection of arterial blockage progression can be integral to preventing PVD, heart attacks, and strokes.

(B) Occluded arteries result in major changes to arterial pressure and can be monitored using a pressure sensor.

(C) The sensor is wrapped around the artery for monitoring of arterial health.

(D) An exposed view illustration of the sensor with the inductor coil for wireless data transmission and interdigitated fringe field capacitive sensor to wrap around the artery. Note: the cross-sectional view is not drawn to scale.

(E) Image of the fabricated device (left) with a scanning electron microscope image of the PDMS pyramid microstructures (right).

over $250 million annually in the United States alone (Khoury et al., 2019). Further, approximately, 10% of patient outcomes resulted in cardiovascular deaths within that time. Sensors inserted during carotid endarterectomy or carotid artery bypass surgeries would target prevention of strokes. Thus, 4–5% of operations have primary outcomes of non-fatal stroke within just the first 30 days of a carotid endarterectomy with increased rates including fatalities (Knappich et al., 2019; Tu et al., 2003). Further, the 1-year risk of stroke is 5.1% and the 5-year risk is 9.4% (Bonati et al., 2015). With over 100,000 people undergoing a carotid endarterectomy annually, this translates to over 9,400 patients whose strokes could be prevented (Lima et al., 2020). Early detection of PVD would be targeted by the insertion of a sensor during a lower extremity bypass surgery. Notably, these statistics do not include the outcomes that were prevented from earlier detection of traditional surgical site monitoring. Current postoperative monitoring (e.g., Doppler flow imaging) after the initial hospital stay is infrequent, and there is no method of monitoring the artery in between in person clinical evaluations. For example, in a femoro-femoral artery bypass surgery, a subset of lower extremity bypass surgery, annual clinical follow-ups are recommended meaning there is no monitoring in between these yearly appointments (Lane et al., 2011). Thus, continuous, long-term monitoring can help prevent recurrent diseases through early detection. This sensor will be able to detect changes in pressure within the artery to notify the patient of a need for further testing "before" symptoms arise.

Here, we present a sensor design and fabrication for wireless, battery-free monitoring of arterial blood pressure that can be applied to a wide range of artery types and sizes during key surgical procedures. The thin and flexible design makes it versatile for large ranges in arterial size and locations of implantation.

Since we will not know the location of the pressure buildup relative to the sensor in these cases, it is important to be able to monitor a wide range of distances both upstream and downstream of the sensor. We designed simple methods to predict sensor performance in vitro to account for changes in arteries and partial to complete occlusion. Wireless operation was enabled using a well-established radio-frequency coupling method for continuous monitoring. The operation of the sensor is further shown in a human cadaver and in vivo in a rat model, for which the sensor demonstrated excellent response to progressive arterial occlusion, biocompatibility, pulse monitoring, and long-term arterial monitoring.

RESULTS

Biocompatible sensor design

We developed an implantable sensor that wraps around an artery to detect changes in blood flow across a wide range of arteries. First, we designed a sensor that is sensitive in the pressure sensing regime but also capable of detecting changes when the artery is in its proximity (Figure 1D). Proximity sensors measure the distance an object is from the sensor prior to contact. In this case, we used a capacitive pressure sensor where the electrodes are planar to capitalize on the capacitive fringe field. We previously demonstrated both computationally and experimentally that fringe-field sensors are capable of proximity sensing by objects disrupting the fringe field (Ruth et al., 2020a). In this case, we used an interdigitated electrode design to increase the number of fringing capacitances, thus increasing the strength of the electric field and consequently the proximity sensing sensitivity. This is important because depending on the diameter of the artery and its location in the body, the sensor may only come in partial contact with the artery when surgically implanted. We use pyramidal elastic microstructures since they significantly increase sensor sensitivity compared to bulk material and other microstructure shapes (Figure 1E) (Mannsfeld et al., 2010; Ruth et al, 2019, 2020a, 2020b; Ruth and Bao, 2020).

We selected a material with well-established biocompatibility to reduce the timeline to eventual implementation (Figure 1D). Polydimethyl siloxane (PDMS) at a 10:1 PDMS to cross linker weight ratio, chosen as the packaging or encapsulation material, has demonstrated strong biocompatibility in vivo and is even used as a reference for new materials (Bélanger and Marois, 2001; Irimia-Vladu, 2014; Victor et al., 2019). We use a polyimide substrate (thickness 80 μm), which has demonstrated in vitro and in vivo biocompatibility (Hiebl et al., 2010; Richardson et al., 1993; Sun et al., 2009). We chose a lower-modulus PDMS (23:1) for the pressure-responsive element because of its biocompatibility, low compressive modulus for high pressure sensitivity, and negligible pressure response hysteresis (Beker et al., 2020; Ruth et al., 2020a). In this work, we found non-statistically significant differences in terms of tissue inflammation between PDMS, polyimide, poly(octamethylene maleate (anhydride) citrate (POMaC), and control at 1 week and 12 weeks (Figure S1; Tables S1 and S2). POMaC is a biodegradable material that demonstrated high biocompatibility in previous studies chosen here to compare our material with a biodegradable material (Boutry et al, 2018, 2019; Oda et al., 2020). Finally, we chose copper for the electrodes, electrical interconnect, and wireless antenna, due to its easy fabrication, high electrical conductivity required for wireless communication, and biocompatibility. Copper has historically used in implanted devices for over 50 years (Zipper et al., 1969). In fact, copper has demonstrated anti-inflammatory properties in implants (Dollwet et al., 1981). However, it is important to note that the copper layer is fully encapsulated by the PDMS and, thus, is not expected to come in contact with the body. With the low material cost per sensor of less than $1, our implantable device is economical, with potential for further cost reduction.

Next, we characterized the sensors and confirmed reproducibility and stability of sensor performance (Figure 2). First, sensor performance was found to be consistent over 20 sensors with a sensitivity (S) of $0.015 \pm 0.0035\ kPa^{-1}$ at 0–3 kPa, $0.0022 \pm 0.00049\ kPa^{-1}$ at 3–38 kPa, and $0.00038 \pm 0.00011\ kPa^{-1}$ at 38–100 kPa (Figure 2A). This demonstrates the reproducibility of the sensor fabrication and consistency of its performance. Second, the sensor reproducibly responds to tens of thousands of cycles over more than 24 h (Figure 2B). Furthermore, the sensor response is stable over 30 days even when submerged in water after an initial period—less than 2 days—of equilibration (Figures 2C–2F). The pressure and proximity capabilities remained intact, demonstrating its performance stability over at least 30 days (Figures 2D–2F).

In vitro design and sensor characterization

The sensors were characterized using three in vitro environments to recapitulate in vivo environments: pulsatile air pump, continuous-flow water pump, and continuous-flow water pump with pulsations from a robotic gripper. The goal of these studies is to evaluate the relevance and versatility of the sensor to monitor

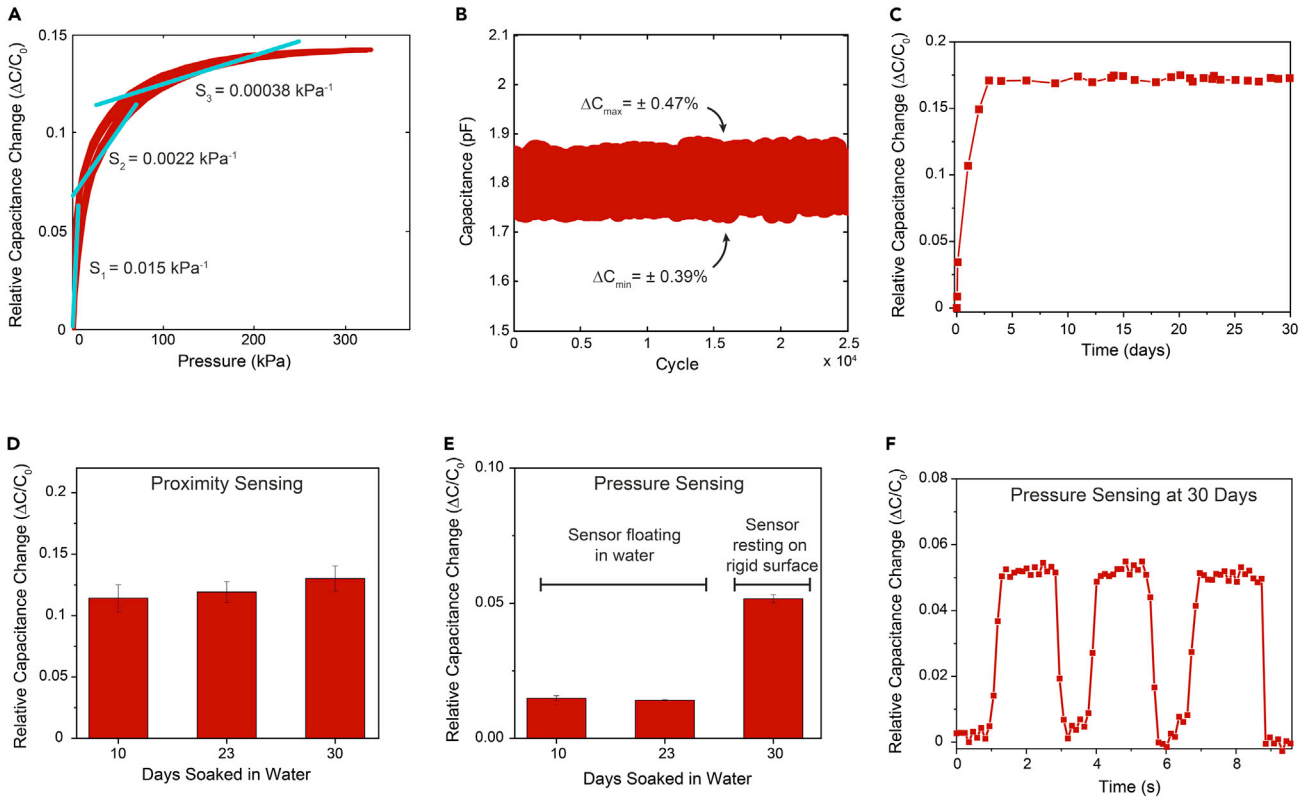

Figure 2. Interdigitated fringe field electrode design with pyramid microstructures demonstrates strong and stable performance capabilities

(A) Relative capacitance changes with respect to applied normal pressure for the interdigitated fringe field capacitive sensors over 5 cycles for one sensor show multiple levels of pressure sensitivity at different pressure ranges.

(B) Cycling test and stability of the pressure response (1 N applied force). The ΔC_{max} and ΔC_{min} refer to the deviation from the average values of the maximum and minimum capacitances, respectively.

(C) After an initial increase in capacitance when the sensor is placed in water, it has a stable signal for at least 30 days. The baseline is the capacitance of the sensor prior to placement in the water.

(D) The mean sensor proximity response was stable over 30 days in water with error bars representing the standard deviation of the relative capacitive change for 3 repetitions. This was done by moving rubber-tipped tweezers toward the water surface, where the sensor was less than 1 mm below the water surface.

(E) The sensor maintained its pressure sensing capability in water over 30 days, with a stable increase in capacitance as a small pressure was applied with rubber-tipped tweezers onto the sensor floating less than 1 mm below the water surface. On day 30, the pressure sensing was measured by applying a light pressure with the rubber-tipped tweezers when the sensor was resting on a rigid surface rather than floating in the water. Error bars represent the standard deviation of the relative capacitive change for 3 repetitions.

(F) The sensor demonstrates a stable response to a small pressure being applied with rubber-tipped tweezers when the sensor was resting on a rigid surface.

a wide range of artery types and sizes and to predict its in vivo efficacy. In this in vitro study, we target 5 major arteries: radial, coronary, carotid, femoral, and popliteal. The radial artery, whose inner diameter is 2.2–3.03 mm, is most often monitored in the intensive care unit (Korten et al., 2007; Madssen et al., 2006). Blockages in the coronary artery lead to coronary artery disease and heart attacks. The left main coronary artery has a typical diameter of 3.38–6.14 mm in 15- to 34-year-old males (Leung et al., 1991). The popliteal artery is often associated with PVD and has a typical diameter of 4.8–7.6 mm (Sandgren et al., 1998). Also, commonly associated with PVD is the common femoral artery with an average diameter of 6.6 mm (3.9–8.9 mm) (Spector and Laweson, 2001). The carotid artery, with a 6.3–7.5 mm diameter in 15- to 25-year-old males and females, is associated with carotid artery disease which can lead to stroke (Hansen et al., 1995).

Thus, to mimic these five arteries, we use either polyolefin tubes or artificial arteries (Syndaver) with inner diameters ranging from 2 to 7 mm. First, we use a pulsatile air pump with physiological pulsation rates with an attached 5- or 6-mm internal diameter (ID) polyolefin tube closed at one end (Figure 3A). With the sensor wrapped around the polyolefin tube, it responded to fluctuations at each of the frequencies and can distinguish between the different frequencies relevant to cardiac pulsations (Figure 3B). To better mimic human

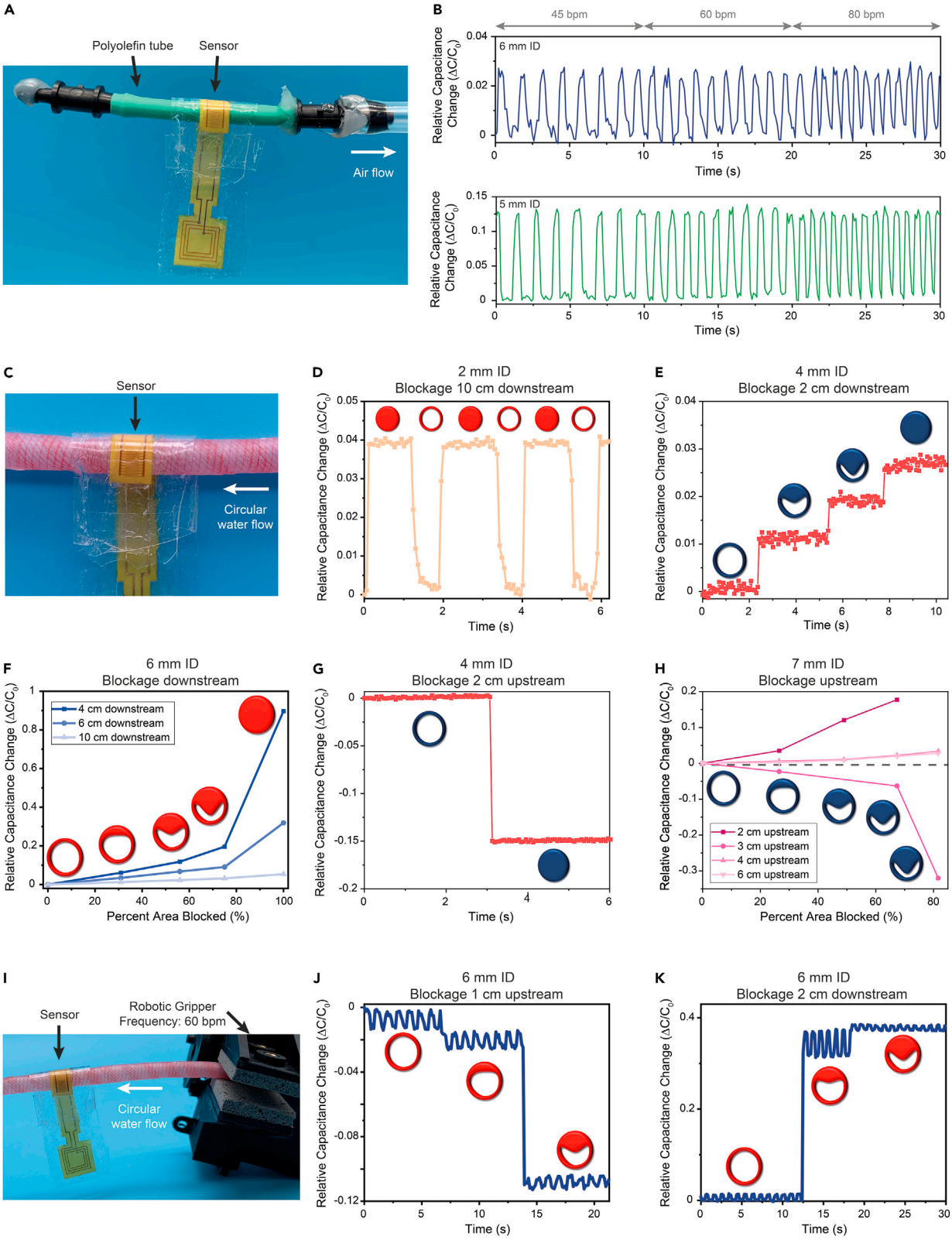
A
Polyolefin tube
Sensor
Air flow
B
45 bpm
60 bpm
80 bpm
6 mm ID
Relative Capacitance Change (ΔC/C0)
Time (s)
5 mm ID
C
Sensor
Circular water flow
D
2 mm ID
Blockage 10 cm downstream
E
4 mm ID
Blockage 2 cm downstream
F
6 mm ID
Blockage downstream
4 cm downstream
6 cm downstream
10 cm downstream
Percent Area Blocked (%)
G
4 mm ID
Blockage 2 cm upstream
H
7 mm ID
Blockage upstream
2 cm upstream
3 cm upstream
4 cm upstream
6 cm upstream
I
Sensor
Robotic Gripper
Frequency: 60 bpm
Circular water flow
J
6 mm ID
Blockage 1 cm upstream
K
6 mm ID
Blockage 2 cm downstream

Figure 3. In vitro demonstrations indicate strong capability to monitor arterial pulsations and arterial blockage progression

(A) Photograph of the experiment setup with the pulsatile negative air flow simulation to mimic arterial pulsatile behavior. The interdigitated fringe-field capacitive sensor is wrapped around a polyolefin tube with either a 5- or 6-mm diameter that is closed at one end and connected to the air pump at the other.

(B) Relative capacitance change of the wired sensor wrapped like a cuff around the artificial artery. The sensor distinguishes between different physiological pulse rates (45, 60, and 80 bpm) when wrapped around the 6-mm tube (top). This capability is consistent for a 5-mm artery even with the addition of a 1-lb layer of artificial fat, skin, and muscle (Syndaver) on top of the construct to better mimic implantation (bottom).

(C) Photograph of the experiment setup with a continuous water flow in a closed circular loop. The interdigitated fringe-field capacitive sensor is wrapped around an artificial artery (Syndaver) with an inner diameter of 2–7 mm. The sensor is wrapped around the artery like a cuff and 1-lb of artificial fat, skin, and muscle is applied on top to mimic for similar additional pressures in vivo. The blockage is incorporated by wrapping a thick rubber string around the artificial artery at different diameters.

(D) The sensor responds to blockages 10 cm downstream of the sensor when wrapped around a 2-mm inner diameter artificial artery to mimic a radial artery. The red-filled circle indicates a blocked artery while the circle with non-filled circle indicates normal flow.

(E) The sensor responds to progression of arterial blockages at 0%, 44%, 75%, and 100% reduction in arterial area when wrapped around a 4-mm inner diameter artificial artery to mimic a coronary artery. The extent of blockage is represented by the extent to which blue circles (to represent an artery) are blue filled.

(F) When wrapped around a 6-mm inner diameter artificial artery to mimic the carotid artery, the sensor demonstrates capability to detect extent of arterial blockage for partial and full blockages up to at least 10-cm downstream of the sensor. Extent of blockage is indicated by extent of red filling of the circles to represent arteries. Data are represented as mean change.

(G) The sensor is able to detect blockages upstream of the sensor, here wrapped around a 4-mm inner diameter artificial artery. Capacitance decreases with application of a blockage to indicate the pressure decrease from elimination of flow.

(H) When wrapped around a 7-mm inner diameter artificial artery to mimic the femoral artery, the sensor demonstrates capability to detect extent of arterial blockage for blockages at different distance upstream of the sensor. The sign of the relative capacitance change is dependent on the distance from the partial blockage due to high-frequency oscillations in flow and pressure. Extent of blockage is indicated by extent of red filling of the circles to represent arteries. Data are represented as mean change.

(I) Photograph of the experiment setup with continuous water flow in a closed circular circuit, similar to (C) with the addition of a robotic gripper (Lynxmotion Little Grip Kit, Robotshop). The gripper was used to introduce pulsations at a rate of 60 bpm with a change in arterial area of 10–15%.

(J) When wrapped around a 6-mm inner diameter artificial artery, the sensor distinguishes between pulses and progression of blockages for a partial blockage 1-cm upstream of the sensor.

(K) When 1-lb of artificial fat, skin, and muscle is applied to the sensor wrapped around a 6-mm inner diameter artificial artery, it still maintains capability to distinguish between pulsations and progression of blockages, here shown for a partial blockage 2-cm downstream of the sensor.

application, we demonstrate the response of the sensor to the pulsations of the polyolefin tube with 1-lb of artificial fat, skin, and muscle overlying the sensor (Figure 3B). Sensor response was actually stronger in the case, likely due to the closer contact between the sensor and the polyolefin tube. This allowed us to observe our sensor's response to fluctuations, but some information is not gained with this system. For example, the flow is not circular as it is in the body, the polyolefin tubes do not perfectly mimic the mechanical properties of arteries, only air is running through the tubes, and air is being sucked out of the system instead of being pumped into the system, as is the case in the body.

To address some of these issues, we used a continuous flow water pump and an artificial artery made for synthetic cadavers to mimic arteries (Figure 3C). Here, the flow is circular so we can monitor partial and full occlusions in the arteries in the form of stenoses with our sensor. We apply 1-lb of artificial fat, skin, and muscle layered on top of the sensor wrapped around the artificial artery to better mimic a general in vivo environment. Sensors were evaluated wrapped around various artery diameters, i.e., 2-, 4-, 6-, and 7-mm ID artificial arteries. All artificial arteries were 12–15 cm in length. Taking into account connectors and the width of the sensor, the furthest possible distance from the sensor for analysis was 10 cm. Since the clinical target for the sensor is to be implanted at the surgical site but not along the entire length of the artery, we confirm the sensor's capability to respond to blockages up to 10 cm upstream and downstream of the sensor. For occlusions downstream of the sensor, an increase in capacitance is expected due to the pressure buildup (Figure 1B). With blockages up to 10 cm downstream of the sensor, the sensor was able to detect them on all four artificial arteries tested (Figures 3D and S2). When there is a full blockage downstream of the sensor, it is expected to cause an increase in capacitance due to the pressure increase upstream where the sensor is located (Figueroa et al., 2006). It is important to note that despite the limitation in the in vitro setup to assess the sensor's capabilities to respond to blockages more than 10 cm from the sensor, the clear response up to that distance indicates that the sensor can likely detect blockages beyond 10 cm away.

Our sensor is able to monitor the progression of arterial blockages from a wide range of distances both upstream and downstream of the sensor. This is important since we will not know exactly where the occlusion will be relative to the sensor in a clinical application and the goal is to be able to monitor arterial health prior to a complete blockage and even prior to the patient experiencing symptoms. Despite the sensor capability to monitor extent

of occlusion even up to at least 10 cm upstream of the partial or full blockage, we observe that the closer the sensor is to the blockage, the stronger the signal response as expected (Figures 3E, 3F, and S3). For partial occlusions upstream of the sensor, the sensor response is dependent on the distance from the blockage. Downstream of a stenosis, the vessel wall changes in response to high-frequency oscillations in flow and pressure (Figure 1B) (Figueroa et al., 2006; Mancini et al., 2019). This is due to the turbulent flow downstream of the stenosis and maintained partial flow through the artery (Beach et al., 2010; Mancini et al., 2019). In the region of the artery experiencing the peak of the oscillations, the measured sensor response is expected to have an increase in capacitance, while other regions of the artery are expected to have a decrease due to the decrease in flow and pressure from the stenosis. However, in all cases, the pressure and capacitance are expected to decrease when the artery is fully occluded upstream of the sensor due to the elimination of flow in the sensor area. When the occlusion is up to 10 cm upstream of the sensor, the sensor can indeed detect full arterial blockages (Figures 3G and S4). However, we observed that the distance of the partial occlusion from the sensor determines the magnitude of the signal (Figure 3H). Notably, in Figure 3H, when the partial occlusion is 3 cm upstream of the sensor, the sensor was likely between peaks of the high-frequency oscillations, so there is an observed capacitance drop. In all cases, though, the sensor was able to detect changes in the extent of occlusion, which predicts its ability to do the same in vivo and early detection of arterial occlusion prior to the patient experiencing symptoms. One of the major limitations of this in vitro testing system is the lack of pulsations that the human body exhibits.

To address this limitation, we introduced oscillations to the same circular flow system using a robotic gripper programmed to oscillate at a frequency of 60 s^{-1} with percent variation in diameter of 10–15%, within the normal range of the popliteal and carotid arteries (Figure 3I) (Buntin and Silver, 1990; Hansen et al., 1995). Even when adding pulsations with the continuous flow system, our sensors were able to detect changes during partial arterial blockages (Figures 3J and 3K). For Figure 3J, the artery was partially occluded 1 cm upstream of the sensor with 30% and 56% reduction in area. The pulses are clearly distinguishable from the changes due to the reduction in area within the artificial artery. When 1-lb. of artificial fat, skin, and muscle were layered on top of the sensor wrapped around the artificial artery, the signal response was stronger (Figure 3K). In this case, the stenosis was 2 cm upstream of the sensor, and the artificial artery was monitored at full flow, 44% reduction in area, and 66% reduction in area. In all three states, the sensor can detect the pulsations while also maintaining the capability to distinguish between the states. Based on observations from the above three in vitro environments, we predicted that our sensors will be capable of monitoring arterial pressure in vivo.

Wireless sensor design and evaluation

To improve patient comfort and long-term risk of infection, we designed a resistor-inductor-capacitor (RLC) circuit to allow wireless monitoring (Figure 4A). The wireless circuit consists of the capacitive pressure sensor connected in series with an inductor coil. The resonance frequency of the LC circuit is determined by the value of capacitance (C) and inductance (L). In our previous work, the capacitive pressure sensor had an initial capacitance of 1.79 $\pm$ 0.15 pF (Ruth et al., 2020a). We then designed a miniaturized antenna coil with the dimensions <1 mm $\times$ 1 mm for minimally invasive surgery. We targeted ~100 nH to achieve the LC resonance frequency of <1 GHz. The resulting range of the LC resonance frequency is 300–400 MHz, which meets the system requirement for wireless communication with the miniature vector network analyzer (mini-VNA).

The frequency of the RLC resonator is inversely proportional to the square root of the capacitance (Figure 4A). Thus, when a pressure is applied, the capacitance should increase, and the frequency should decrease in our wireless device. To monitor these shifts wirelessly through the skin, inductive coupling is employed with an external reader coil for which the scattering parameter S_{11} is measured. When 100 g or 12.5 kPa was applied to the sensor, the frequency decreased, and this response was reversible as we remove or load the weight (Figure 4B). This was repeated with different pressures (0, 0.011, 0.13, 0.26, 0.64, 1.3, 2.5, 6.3, and 12.5 kPa) using 10 different sensors to determine the frequency change as a function of pressure (Figures 4C and 4D). In all cases, as the pressure increased, the frequency decreased.

Further, we confirmed that the suggested LC sensor showed reasonable sensing performance enough to monitor arterial pulsations and arterial blockage progression. The wireless sensor was evaluated in the in vitro environment to confirm reliability and stability. In this case, we used the in vitro environment with a continuous-flow water pump connected to artificial arteries (Figure 3C) and evaluated under the pressure of 1-lb of artificial fat, skin, and muscle layered on top of the sensor wrapped around the artificial artery. Then, 1-mm thick artificial skin (Syndaver) was also placed on the antenna to better anticipate the sensor

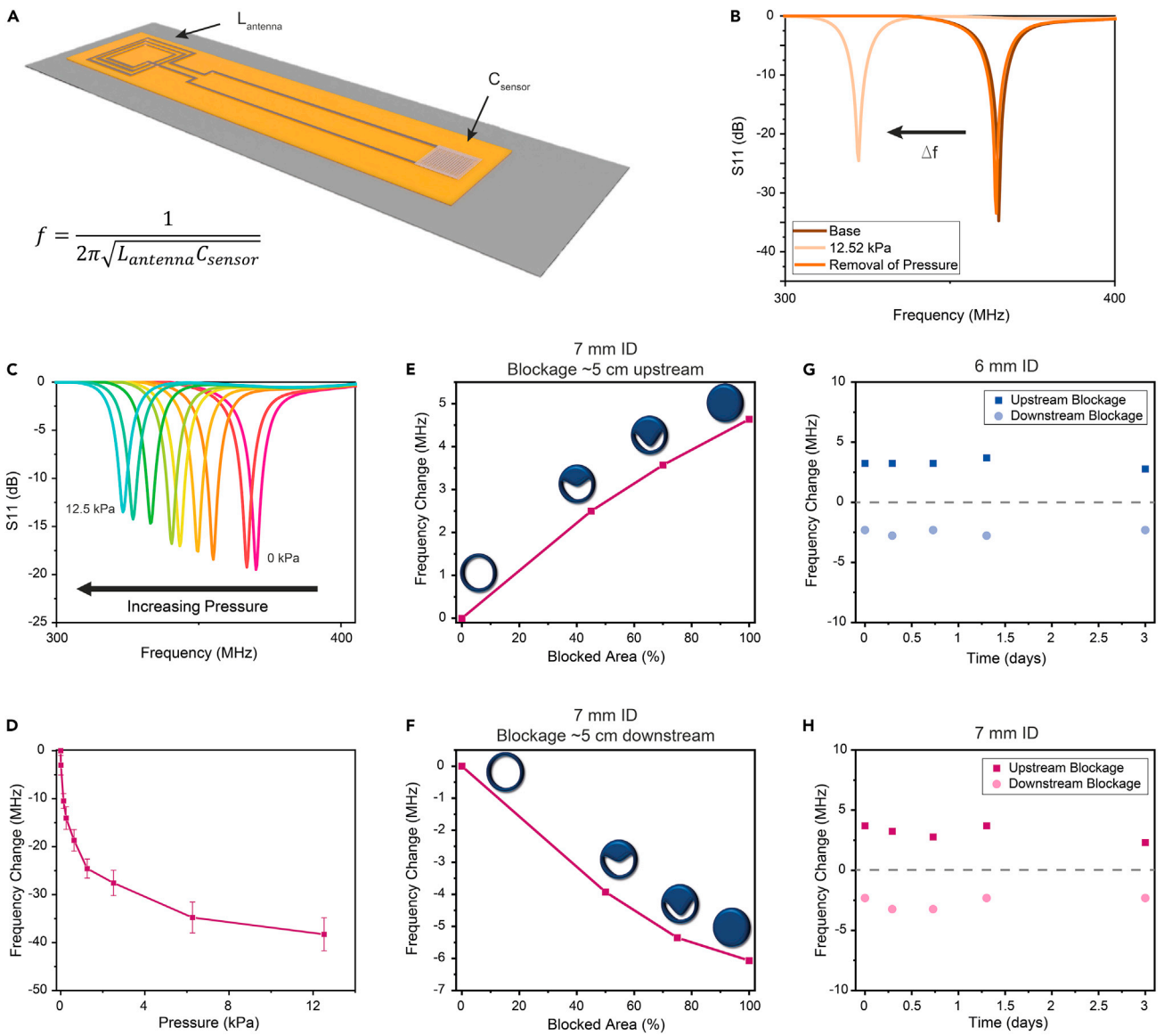

Figure 4. Wireless sensor performance is reliable and stable in in vitro environments

(A) The design for the full wireless interdigitated fringe field capacitive sensor.

(B) Applied pressure causes a negative shift in frequency. Here, demonstrated with the addition of 12.52 kPa, the response to applied pressure is reversible.

(C) The sensor responds to increasing pressure, shown here from 0 kPa to 12.52 kPa.

(D) The wireless sensor response to applied pressure is consistent over 10 sensors. Error bars indicate one standard deviation from the mean.

(E) The wireless sensor was tested on the in vitro environment described in Figure 3C with a 1–2-mm-thick artificial skin layer (Syndaver) added on top of the wireless antenna to mimic detection through the skin. The wireless sensor demonstrates the same capability to respond to progression of arterial blockages when the blockage was 5-cm upstream. The extent of blockage is represented by the extent the blue circles (to represent an artery) are blue filled. Data are represented as mean change.

(F) In the same in vitro environment described in (E), the sensor also responded to progression of arterial blockages when the blockage was 5-cm downstream. Data are represented as mean change.

(G) The sensor was wrapped around an artificial artery for 3 days and stored in water. Its response to blockages both upstream and downstream of the sensor was stable over this time when wrapped around the 6-mm inner diameter artificial artery. Data are represented as mean change.

(H) When the same experiment as in (G) was repeated with a 7-mm inner diameter artificial artery, the sensor response to blockages was stable over the 3 days monitored. Data are represented as mean change.

response through the skin in vivo. The wireless sensor was found to be responsive to progression of blockages within the artificial artery for blockages both upstream and downstream of the sensor (Figures 4E and 4F). When the partial blockage is upstream of the sensor, there is a pressure decrease from lack of flow where the sensor is placed resulting in a decrease in capacitance and, consequently, an increase in frequency. The opposite is true when a partial blockage is downstream of the sensor. In this case, there is pressure buildup from the prevention of flow by the occlusion causing an increase in capacitance and, consequently, a decrease in frequency.

To evaluate stability of the sensor wrapped around an artery, a wireless sensor was wrapped around the 6- and 7-mm ID artificial arteries for 3 days and stored in water (Figures 4G and 4H). This was done to determine whether the sensor would be stable when implanted around an artery and further evaluated in later in vivo studies. In both cases, the sensor performance was evaluated with 1-lb artificial fat, skin, and muscle layered on the sensor and 1-mm skin on the antenna to better mimic in vivo environments. The sensor response to partial blockages both upstream and downstream of the sensor was found to be stable over 3 days for both artificial arteries (Figures 4G and 4H). Once again, we observed an increase in frequency when the blockage was upstream of the sensor due to the decrease in capacitance from the prevention of flow to the sensor area. The sensor frequency decreased when the blockage was downstream of the sensor due to the pressure buildup and consequent capacitance increase.

Occlusion monitoring on a human cadaver

To examine how the sensor would perform in a human, we applied the sensor around the femoral artery of a human cadaver. Salt (NaCl) water (0.15–0.2 M) flowed through a physiologically accurate pulsatile water pump at a rate of 60 beats per minute (bpm) to mimic normal human blood flow pulse rate through the artery. Salt water was used because it has a similar dielectric constant and electrical conductivity to blood (Gabriel et al., 1996; Gadani et al., 2012; Gavish and Promislow, 2016; Jaspard et al., 2003; Widodo et al., 2018). The sensor was wrapped around the femoral artery (Figures 5A and 5B) and monitored wirelessly using a mini-VNA. For this study, we opened most of the length from the hip to the knee to be able to examine the sensor's ability to detect partial and complete occlusions both upstream and downstream. To maintain access to occluding the vessel, the incision on the leg remained open for the duration of the study unless otherwise specified. However, for clinical application, the sensor will be applied at a location on the artery that is already visualized during surgery and implantation of the sensor would not require additional surgery or surgical incisions. Due to the lack of continuous measurement capability of the mini-VNA, we averaged each condition over 5 data points to account for fluctuations due to pulsations within the artery with standard deviation as the error bars.

Since the location of the occlusion cannot be anticipated in PVD, carotid artery disease, or other arterial diseases, we examined the sensor response to occlusions both upstream and downstream of the sensor. When the occlusion was placed 8.5 cm downstream of the sensor, the sensor detected the expected pressure buildup as indicated by the wireless sensor frequency decrease (Figure 5C). As the artery becomes more occluded due to the downstream blockage, the salt water built up upstream of the blockage, where the sensor was located. This led to an increase in capacitance due to the increase in pressure and thus a decrease in frequency change. Notably, this length includes both the common and superficial femoral arteries (Schneider et al., 2008). When the occlusion was placed 2.7 cm upstream of the sensor, the sensor was able to detect changes in the extent of occlusion (Figure 5D). Due to high-frequency oscillations in flow and pressure, the sensor detected an increase in pressure when the artery was partially occluded. However, full occlusion restricted any flow to the sensor area, thus decreasing the pressure within the artery. This decrease in pressure results in a decrease in capacitance of our sensor and thus an increase in frequency change. Thus, our sensor is able to detect the progression of occlusion in the common and superficial femoral arteries over at least 11.2 cm in length. Although it is difficult to anticipate where a blockage will occur, the tested region spanned the length of the thigh in the cadaver studied and we predict from additional in vitro studies that our sensor can sense over at least 40 cm in length—20 cm upstream and 20 cm downstream (Figure S5). This was done by suturing together two 6-mm ID artificial arteries and monitoring response to the progression of arterial occlusion. Measuring by the average length of the femur—40 cm for women and 45 cm for men—the sensor is capable of monitoring the entire vessel after a femoral popliteal lower extremity bypass (Holtby, 1918; Pick et al., 1941). Based on the surgeries discussed in this work, this would be the longest distance we would be monitoring since the carotid and coronary arteries are both shorter than the distance monitored after this surgery. Being able to detect an occlusion over large

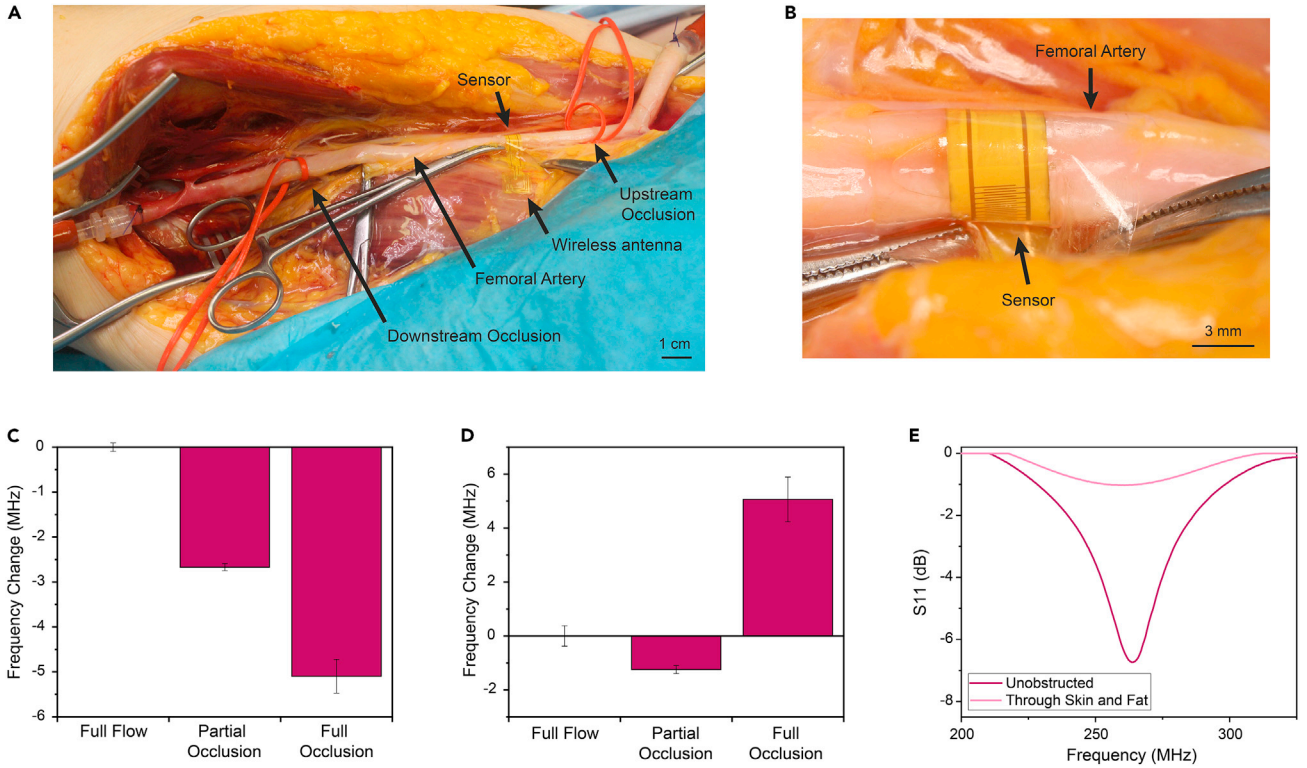

Figure 5. The arterial sensor demonstrates capability to monitor arterial occlusion in the femoral artery in a human cadaver

(A) Image of the implantation site with the wireless sensor wrapped around the human femoral artery. A VNA was used to monitor the frequency change of the wireless device.

(B) Close-up view of the implantation site showing the placement of the wireless device wrapped around the artery.

(C) The wireless sensor responds progressively to partial and full occlusions 8.5 cm downstream of the sensor. Error bars indicate the range of the sensor response to pulsations for each condition, indicating signal variation due to arterial pulsations.

(D) The wireless sensor responds to progression of arterial occlusion 2.7-cm upstream of the sensor. Due to the high-frequency oscillations in flow and pressure, a partial occlusion causes a decrease in frequency indicating an increase in pressure. Error bars indicate the range of the sensor response to pulsations for each condition, indicating signal variation due to arterial pulsations.

(E) Although there is a signal loss when reading the sensor antenna through the skin and ~1-cm of fat layer, there is still a clear signal that can be used for monitoring.

distances from the sensor is vital for this case since the placement of the sensor will be dependent on the surgery the patient is undergoing and it is difficult to predict the relative distance from the sensor that a possible occlusion would occur.

To ensure wireless readout capability through the skin and fat in the leg, we placed the sensor antenna approximately 1 cm beneath the skin surface, surrounded by fat. There was still a clear signal detected through 1 cm of fat and skin in the leg (Figure 5E). For clinical applications, implanting the sensor antenna in a pocket directly underneath, the skin will be desirable for the strongest signal, as further discussed in the in vivo monitoring section. In this case, we were restricted to the predetermined length of the fabricated sensor, which did not accommodate for the full distance to place the antenna directly beneath the skin. To accommodate this in a clinical setting, the wire length between the sensor and its antenna can be easily adjusted with standard sizes available based on vessel diameter and location of implantation.

In vivo arterial pressure monitoring

As previously discussed, prior to in vivo testing of the entire device, we evaluated the biocompatibility of the packaging material along with the polyimide substrate. The goal of this work is to verify proper operation of the sensing fringe-field capacitor for arterial blockage monitoring, biocompatibility of the entire sensor, and to validate wireless signal monitoring capability through the skin on a live small animal model. The rat femoral artery is significantly smaller than human radial, femoral, or carotid arteries and exhibits

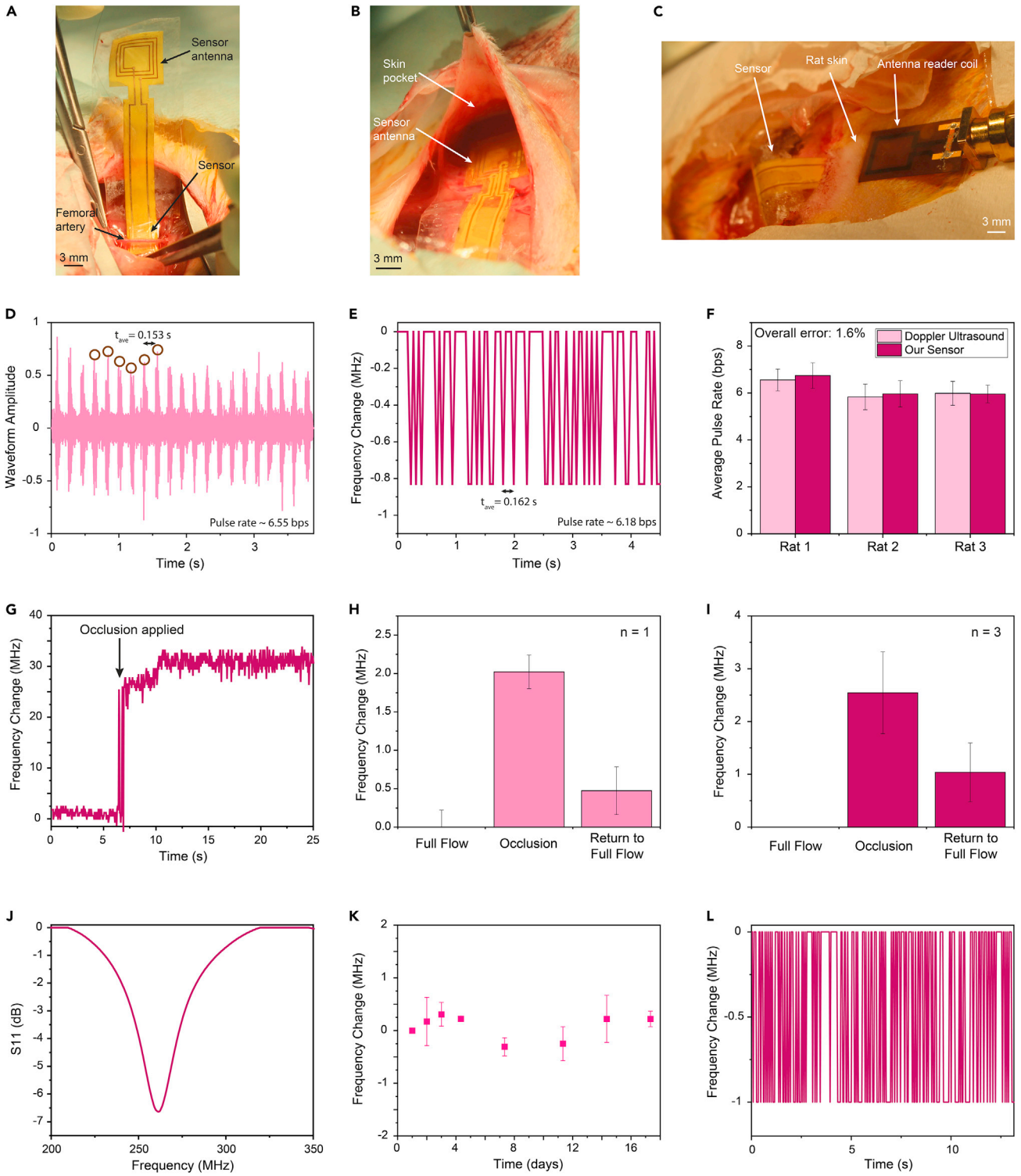

Figure 6. The arterial pressure sensor demonstrates strong capability for monitoring arterial occlusion in vivo for over 2 weeks

(A) Image of the implantation site with the wireless sensor under the femoral artery. This was followed by fully wrapping the sensor like a cuff and suturing on each side.

(B) Image of the wireless antenna placed in the skin pocket that was made during the surgery.

(C) Image of the testing setup when the sensor was wirelessly monitored through the skin while still having access to occlude the femoral artery.

Figure 6. *Continued*

(D) Sound waveform of the external Doppler ultrasound measured through a microphone; the pulse rate was determined to be ~6.55 bps. This was repeated for each rat.

(E) When monitoring the sensor wirelessly through the skin, the sensor maintained its ability to respond to pulsations in the artery. The pulse rate was calculated to be 6.18 bps.

(F) The pulse rate calculated from the Doppler ultrasound for each rat is compared to the pulse rate calculated from the wireless sensor readout. The overall error is 1.6%. Data are represented as mean change +/− SEM.

(G) When the sensor has good contact with the artery, the response to partial arterial occlusion is strong.

(H) The sensor response to partial arterial occlusion using surgical clamps was wirelessly monitored with the mini-VNA through the skin of the rat. Error bars indicate the range of the sensor response to pulsations for each condition, indicating signal variation due to arterial pulsations.

(I) The sensor response to partial arterial occlusion wirelessly monitored with the mini-VNA through the skin of the rat was consistent (n = 3). Error bars indicate one standard deviation from the mean.

(J) The signal through the skin of the rat a day after implantation was strong.

(K) The signal of the sensor was stable and consistent for the three rats over 17 days with frequency changes within the range for changes due to pulsations. Error bars indicate one standard deviation from the mean (n = 3).

(L) Even 2 weeks after implantation, the wireless sensor stably monitors the pulsations in the femoral artery.

smaller changes in pressure than the human femoral and carotid arteries. Further, due to the smaller anatomy of the rat, more movement of the sensor is expected in the rat as compared to a human, especially since the sensor is implanted near a joint in the case of the small animal model. In addition, the pulsatile behavior of the rat femoral artery is similar to that seen in human arteries but with a much higher frequency. Male Sprague-Dawley rats that are single housed as used in this study have heart rates approximately 300–400 bpm, while human resting heart rates are less than one-quarter of that (Azar et al., 2011). Smaller animal models have smaller vessels and smaller changes in vessel diameter. Thus, by choosing a smaller animal model, we ensure the sensor would perform well even on small human vessels with smaller changes in diameter, stiffer vessels with less vasodilation, and in patients with tachycardia. We anticipate that the performance of the sensor wrapped around the rat femoral artery represents the minimal performance it would exhibit in a human.

Figures 6A–6C show the experimental design of the in vivo arterial-pulse monitoring with the wireless sensor implanted in a rat. A sensor with the dimensions 6 mm × 55 mm was wrapped around the femoral artery of a Sprague-Dawley rat, fixed with sutures through the PDMS on each side of the sensor (Figure 6A). The experiment was also repeated to confirm the results of the in vivo arterial-pulse monitoring with modifications to the overall length of the PDMS encapsulation layer (~60 mm) to improve flexibility of the overall system, the sensors were fixed with microclips instead of sutures to avoid introducing additional holes to the device, and small branching vessels were clipped to allow some sensor movement along the vessel with leg motion of the rat (Figure S6). All blockages were introduced upstream of the sensor. For long-term monitoring of the sensor and performance characterization through the skin, a skin pocket was created directly beneath the skin layer to achieve the strongest signal from the sensor antenna coil (Figure 6B). The skin pocket allows the sensor to be wrapped around the femoral artery while the antenna coil remained close to the external reader coil to which it was inductively coupled (Figure 6C), and the S_{11} parameter was recorded with a network analyzer and a mini-VNA. The traditional network analyzer was used to monitor pulses for comparison with a Doppler ultrasound (Figure 6D and Video S1). The mini-VNA was used to monitor the sensor similar to the clinical target as it provides a more economic and compact alternative to the traditional network analyzer. With the mini-VNA, we account for changes due to pulsations by taking multiple measurements at a given condition, similar to the human cadaver study.

The external Doppler ultrasound was used to monitor pulse rate for comparison with our sensor (Figure 6D). The pulse rate was calculated by taking the inverse of the average beat-to-beat time over 10 s. We recorded the sound waveform using the Doppler ultrasound and analyzed it to determine the pulse. We also tested the sensor response with the antenna coil placed in the skin pocket, which was easily detectable and found to have a pulse rate of approximately 6.18 beats per second (bps), matching well with the results of the Doppler ultrasound (Figures 6E and S7). We then compared the Doppler ultrasound response to our sensor's response and found that the overall error between our wireless sensor and the Doppler ultrasound was 1.6%, demonstrating a nearly identical response (Figure 6F). The slight difference can be accounted for from having taken the measurements in succession and not simultaneously. When the study was repeated with four additional rats, the results were consistent with only a 1.1% overall error between our wireless sensor and the Doppler ultrasound (Figure S8). This ability to respond to fast pulse rates indicates that our sensor is capable of measuring pulse rates even for patients with tachycardia. Our sensor was also

compared to the commercially available wired Cook-Swartz Doppler Probe, which is generally only used in the hospital for up to 1 week prior to degradation (Figure S9; Video S2). The Cook-Swartz Doppler Probe relies on detection of blockages by changes in the audible signal that must be recognized by the physician. This sensor was implanted around the femoral artery of two rats. The quantitative readout of our sensor provides an advantage over the ultrasound-based commercial sensor in providing more objectivity in processing the sensor readout. Further, we were unable to monitor the Cook-Swartz Doppler Probe beyond the first day because the rats were able to remove the wired sensor, providing an additional advantage in the wireless design of our sensor.

To further demonstrate the performance of the wireless sensor, an occlusion test was performed, whereby the femoral artery was blocked for 15–20 s using a miniature surgical clamp and then released (Figure S10; Video S3). The goal was to evaluate the sensor response to a change in arterial flow. In many medical conditions, plaque buildup or blood clot formation within the vessel slows down the blood flow through the artery. By applying the surgical clamp, we mimicked this condition similar to the stenoses applied in the in vitro and human cadaver studies. Notably, the occlusion was partial to prevent potential post-surgical blood clots. An external reader antenna was again used to monitor the S_{11} parameter with both a VNA and mini-VNA.

The sensors were all evaluated at the time of implant with no barrier between the sensor antenna coil and the reader coil. When the wireless sensor has good contact with the artery, the response is strong (Figure 6G). It can be seen that once the surgical clamps were added, the frequency increased considerably. This increase is due to the decrease in pressure within the artery as it is partially occluded due to decreased blood flow. However, even when the connection to the artery is weaker, the response is still clear (Figure S11). This accounts for potential changes to future movement of the sensor or subject. It can be seen that once the surgical clamps were added, the frequency decreased, and once they were removed, the frequency increased. In this case, there was a decrease in frequency with the addition of the clamps, accounting for the increase in pressure, likely due to the placement of the clamps upstream of the sensor and at the peak of the high-frequency oscillations of pressure and flow. Notably, the artery does not completely return to its original state immediately after the clips are removed due to the viscoelastic properties of arteries (Dorbin, 1978), as can be seen in Figure S11.

The sensor antenna coil was then placed in the skin pocket created for it, and the sensor performance was evaluated to mimic the performance for long-term monitoring through the skin. Notably, our wireless sensor detects partial vascular occlusion through the skin, consistent across all subjects (n = 3). Figures 6H and S12 show the sample results from individual rats, with the error bars indicating the frequency change due to pulsations, as previously discussed. Since the artery does not recover instantly from an occlusion, the frequency does not return to its original value immediately after the partial occlusion is released and full flow is restored. This trend is consistent (n = 3), as shown in Figure 6I, where here error bars indicate the standard error of the frequency changes over 3 rats. This demonstrates proper and consistent operation of the wireless device even when detecting through the skin. This sensor capability was consistent when the in vivo testing was repeated with four additional rats (Figure S13). In fact, even once the surgical site was completely closed, the signal remained strong (Figure 6J), indicating the capability of long-term monitoring through the skin and limiting potential infections at the implantation site by eliminating wires.

The rats were monitored post-implantation for sensor biocompatibility and stability of the sensor response. The subjects were able to move without any apparent limb impairment immediately after recovery from anesthesia (Video S4). Further, to demonstrate function over time, the sensor was implanted and tested continuously. The sensor signal stability was monitored to ensure that any changes to the output signal would be due to changes in the pressure within the artery and not due to drift. The sensor signal was stable over more than 2 weeks (n = 3) with signal changes all within the range of fluctuations due to arterial pulsations (Figure 6K). At 2 weeks from implantation, all implanted sensors were able to detect pulsations from the artery, closely matching the pulse rates obtained by an external Doppler ultrasound (Figures 6L and S14). This is longer than the 1 week use of the current market standard sensor, Cook-Swartz Doppler Probe, and was confirmed when the in vivo study was repeated (Figure S15). In the first round of in vivo studies, the sensors were torn and no longer intact at 3 weeks post-implantation. This was likely due to the interaction between the sensor and surrounding branching small vessels during leg movement and introduction of holes when sutures were used during implantation. In response to this, in a second round of in vivo studies, we made small changes in the length of the sensor encapsulation layer and in the dissection and

implantation of the sensor which resulted in improved stability so that the sensors remained intact for all 3 weeks (Figure S16). In fact, there was a clear response to occlusion by tying off the femoral artery with sutures at explantation (Figure S17). Three weeks post-implantation, the sensor was removed from the rat and samples of the surrounding artery and tissues were investigated for foreign body reactions. No severe inflammation around the sensor implantation site was observed, and histological evaluations showed arterial patency (Figure S18).

DISCUSSION

In this study, we design and fabricate a cost-effective sensor and evaluated its performance characteristics for potential use in early detection of arterial blockages related to PVD, heart attacks, and strokes. Using an interdigitated electrode design and pyramid elastic microstructures, our fringe field sensor has strong pressure and proximity sensing capabilities made of biocompatible materials. We designed three in vitro environments to assess the sensor's capability to monitor physiologic pulsation rates, response to partial and complete occlusions on a wide range of artificial artery sizes, and distinction between pulsation and occlusions of the artery. When the sensor was made wireless, the response and trend were clearly observed with signal detection even through artificial skin. The sensor was further able to respond to partial and full blockages in the femoral artery of a human cadaver that spanned over 11 cm of arterial length upstream and downstream of the sensor. For the in vivo study, we used a small animal model for preliminary evaluation of the sensor performance, stability, and biocompatibility which is more challenging than testing on larger animal models due to the small arterial sizes, weaker signal, and smaller changes in pressure. We monitored the sensor performance in the human cadaver femoral artery to assess the clinical potential with the normal range for a human adult. To further assess the usage of the sensor for carotid artery bypass, carotid endarterectomy, coronary artery bypass, and lower extremity bypass surgeries, we evaluated its response to progression of arterial blockages in vitro 20 cm upstream and downstream of the sensor, spanning at least 40 cm of arterial length. In all cases, post-surgical short-term and long-term monitoring is done around the surgical site to monitor reoccurrence of arterial occlusion. For example, averages of 21.0% of patients have at least a moderate restenosis or occlusion within the first year of an endarterectomy and almost 30% within 5 years of the endarterectomy (Bonati et al., 2018). Additionally, 3-year incidence of restenosis is 39% after lower extremity bypass surgery (Darling et al., 2017). Within the first year after lower extremity bypass surgery, there is a 12% occurrence of a graft occlusion (Goodney et al., 2010). Following a coronary artery bypass, the graft occlusion rate is 4.3% (Hwang et al., 2021). These frequent episodes of restenosis and occlusion do not occur in the same location in each patient, so the ability to monitor long lengths of the artery is crucial for early detection.

Future work includes evaluation on larger animal models to better predict sensor performance in humans with larger arteries and greater distance from joints that cause significant mechanical stress to the sensor. This will also enable evaluation of performance in arteries with longer distances and significant branching, more indicative of performance in humans. Further, the materials may be selected for longer term stability in vivo to limit swelling of the PDMS while maintaining mechanical stability and flexibility of the material. This would be used to ensure stability of the sensor over at least 5 years post-surgery, during which there are higher rates of stenosis, decreased blood flow, and/or clots.

These sensors have strong potential for clinical use with their versatility, commercially available materials, and ease of fabrication. One of the major challenges is in locating the sensor antenna through the skin. First, we anticipate less movement of the antenna in human subjects compared to the rat, meaning the antenna location should be relatively more stable. This is because the much larger size of the human body allows for selection of sensor implantation sites that are less subject to joint motion. Additionally, to make the sensor more applicable in the clinical setting, larger antenna coils can be used. This would provide a larger working range for the sensor. This option was limited in the small animal model due to the small area available for the antenna coil. For human subjects, making a larger antenna coil and implanting it beneath the skin is feasible and would improve the sensor signal detection range. Additionally, although we used one sensor size, we anticipate the use of a larger range of wire lengths and even sensor areas to be customized to the artery size. Since artery sizes vary greatly between patients and even within patients depending on the artery type and the distance between the artery and the skin can vary widely as well, there could be a series of standard sizes of the sensors with different wire lengths be selected from for use clinically. This streamlines the process of fitting the sensor for each patient and makes the sensor more versatile for a wide range of applications.

In summary, this study introduces a biocompatible, wireless, fringe-field capacitive sensor with the potential for long-term monitoring of arterial health on a wide range of arteries for early detection of partial blockages related to stroke, PVD, and heart attacks.

Limitations of the study

Our study is limited in its in vivo evaluation with a focus on small animal models. Although it provides invaluable information about the performance of the sensor in a live model, it is limited in the size and branching of the arteries as compared to humans. Due to the size of the animal, we needed to implant the sensor close to a joint, which would not be done when implanting the sensor in humans. Thus, it limits our capability to accurately predict how the sensor will perform in the patient. Further, this study was limited to 3 weeks, which limits our capability to predict more long-term efficacy of the sensor, which is why we recommend extending the study time in future work. Finally, the study was limited to one antenna coil size, which limits the depth at which the sensor can be implanted.

STAR★METHODS

Detailed methods are provided in the online version of this paper and include the following:

- KEY RESOURCES TABLE
- RESOURCE AVAILABILITY
  - Lead contact
  - Materials availability
  - Data and code availability
- EXPERIMENTAL MODEL AND SUBJECT DETAILS
  - *In vivo* animal models
- METHOD DETAILS
  - Silicon mold fabrication
  - Microstructure fabrication
  - Encapsulation layer fabrication
  - Sensor assembly
  - Normal force testing
  - In vitro testing – Air pump
  - In vitro testing - Syndaver
  - Wireless testing
  - Cadaver model
  - In vivo testing – Sensor function assessment
  - Biocompatibility – Surgery
  - Biocompatibility – Tissue harvest and assessment
- QUANTIFICATION AND STATISTICAL ANALYSIS
  - Statistical analysis

SUPPLEMENTAL INFORMATION

Supplemental information can be found online at https://doi.org/10.1016/j.isci.2021.103079.

ACKNOWLEDGMENTS

The authors thank J.C.R., L.B., and A.A. for discussion on this work. This project is supported by the Beijing Institute of Collaborative Innovation, Plastic Surgery Foundation and American Society for Reconstructive Microsurgery.

AUTHOR CONTRIBUTIONS

Conceptualization and project design, Z.B., P.M.F., and S.R.A.R.; sensor and antenna design, S.R.A.R. and M.-g.K.; device fabrication, S.R.A.R.; experimental design, performance, and analysis, S.R.A.R., M.-g.K., Y.K., Z.W., H.O., and P.M.F.; software and hardware engineering, S.R.A.R., M.-g.K., and Y.K.; supervision, Z.B. and P.M.F.; writing—original draft, S.R.A.R.; writing—review & editing, Z.B., P.M.F., and S.R.A.R.

DECLARATION OF INTERESTS

Authors declare no competing interests.

Received: June 25, 2021
Revised: August 10, 2021
Accepted: August 29, 2021
Published: September 24, 2021

REFERENCES

Alexander, J.H., and Smith, P.K. (2016). Coronary-artery bypass grafting. N. Engl. J. Med. *374*, 1954–1964. https://doi.org/10.1056/NEJMra1406944.

Azar, T., Sharp, J., and Lawson, D. (2011). Heart rates of male and female Sprague-Dawley and spontaneously hypertensive rats housed singly or in groups. J. Am. Assoc. Lab. Anim. Sci. *50*, 175–184.

Beach, K.W., Bergelin, R.O., Leotta, D.F., Primozich, J.F., Sevareid, P.M., Stutzman, E.T., and Zierler, R.E. (2010). Standardized ultrasound evaluation of carotid stenosis for clinical trials: University of Washington Ultrasound Reading Center. Cardiovasc. Ultrasound *8*, 1–15. https://doi.org/10.1186/1476-7120-8-39.

Beker, L., Matsuhisa, N., You, I., Ruth, S.R.A., Niu, S., Foudeh, A., Tok, J.B.H., Chen, X., and Bao, Z. (2020). A bioinspired stretchable membrane-based compliance sensor. Proc. Natl. Acad. Sci. U S A *117*, 11314–11320. https://doi.org/10.1073/pnas.1909532117.

Bélanger, M.C., and Marois, Y. (2001). Hemocompatibility, biocompatibility, inflammatory and in vivo studies of primary reference materials low-density polyethylene and polydimethylsiloxane: a review. J. Biomed. Mater. Res. *58*, 467–477. https://doi.org/10.1002/jbm.1043.

Bonati, L.H., Dobson, J., Featherstone, R.L., Ederle, J., Van Der Worp, H.B., De Borst, G.J., Mali, W.P.T.M., Beard, J.D., Cleveland, T., Engelter, S.T., et al. (2015). Long-term outcomes after stenting versus endarterectomy for treatment of symptomatic carotid stenosis: the International Carotid Stenting Study (ICSS) randomised trial. Lancet *385*, 529–538. https://doi.org/10.1016/S0140-6736(14)61184-3.

Bonati, L.H., Gregson, J., Dobson, J., McCabe, D.J.H., Nederkoorn, P.J., van der Worp, H.B., de Borst, G.J., Richards, T., Cleveland, T., Müller, M.D., et al. (2018). Restenosis and risk of stroke after stenting or endarterectomy for symptomatic carotid stenosis in the International Carotid Stenting Study (ICSS): secondary analysis of a randomised trial. Lancet Neurol. *17*, 587–596. https://doi.org/10.1016/S1474-4422(18)30195-9.

Boutry, C.M., Beker, L., Kaizawa, Y., Vassos, C., Tran, H., Hinckley, A.C., Pfattner, R., Niu, S., Li, J., Claverie, J., et al. (2019). Biodegradable and flexible arterial-pulse sensor for the wireless monitoring of blood flow. Nat. Biomed. Eng. *3*, 47–57. https://doi.org/10.1038/s41551-018-0336-5.

Boutry, C.M., Kaizawa, Y., Schroeder, B.C., Chortos, A., Legrand, A., Wang, Z., Chang, J., Fox, P., and Bao, Z. (2018). A stretchable and biodegradable strain and pressure sensor for orthopaedic application. Nat. Electron. *1*, 314–321. https://doi.org/10.1038/s41928-018-0071-7.

Boutry, C.M., Nguyen, A., Lawal, Q.O., Chortos, A., Rondeau-Gagné, S., and Bao, Z. (2015). A sensitive and biodegradable pressure sensor array for cardiovascular monitoring. Adv. Mater. *27*, 6954–6961. https://doi.org/10.1002/adma.201502535.

Buntin, C.M., and Silver, F.H. (1990). Noninvasive assessment of mechanical properties of peripheral arteries. Ann. Biomed. Eng. *18*, 549–566.

Darling, J.D., McCallum, J.C., Soden, P.A., Korepta, L., Guzman, R.J., Wyers, M.C., Hamdan, A.D., and Schermerhorn, M.L. (2017). Results for primary bypass versus primary angioplasty/stent for lower extremity chronic limb-threatening ischemia. J. Vasc. Surg. *66*, 466–475. https://doi.org/10.1016/j.jvs.2017.01.024.

Dollwet, H.H.A., Schmidt, S.P., and Seeman, R.E. (1981). Anti-inflammatory properties of copper implants in the rat paw edema: a preliminary study. Agents Actions *11*, 746–749. https://doi.org/10.1007/BF01978800.

Dorbin, P.B. (1978). Mechanical properties of arteries. Physiol. Rev. *58*, 397–456. https://doi.org/10.3233/BIR-1982-19303.

Fanari, Z., and Weintraub, W.S. (2015). Cost-effectiveness of medical, endovascular and surgical management of peripheral vascular disease. Cardiovasc. Revasc. Med. *16*, 421–425. https://doi.org/10.1016/j.carrev.2015.06.006. Cost-effectiveness.

Figueroa, C.A., Vignon-Clementel, I.E., Jansen, K.E., Hughes, T.J.R., and Taylor, C.A. (2006). A coupled momentum method for modeling blood flow in three-dimensional deformable arteries. Comput. Methods Appl. Mech. Eng. *195*, 5685–5706. https://doi.org/10.1016/j.cma.2005.11.011.

Forouzanfar, M.H., Liu, P., Roth, G.A., Ng, M., Biryukov, S., Marczak, L., Alexander, L., Estep, K., Abate, K.H., Akinyemiju, T.F., et al. (2017). Global burden of hypertension and systolic blood pressure of at least 110 to 115mmHg, 1990–2015. J. Am. Med. Assoc. *317*, 165–182. https://doi.org/10.1001/jama.2016.19043.

Gabriel, S., Lau, R.W., and Gabriel, C. (1996). Physics in Medicine & Biology. The dielectric properties of biological tissues: III. Parametric models for the dielectric spectrum of tissues. Phys. Med. Biol. *41*, 2271–2293.

Gadani, D.H., Rana, V.A., Bhatnagar, S.P., Prajapati, A.N., and Vyas, A.D. (2012). Effect of salinity on the dielectric properties of water. Indian J. Pure Appl. Phys. *50*, 405–410.

Gavish, N., and Promislow, K. (2016). Dependence of the dielectric constant of electrolyte solutions on ionic concentration: a microfield approach. Phys. Rev. E *94*, 012611. https://doi.org/10.1103/PhysRevE.94.012611.

Goodney, P.P., Nolan, B.W., Schanzer, A., Eldrup-Jorgensen, J., Bertges, D.J., Stanley, A.C., Stone, D.H., Walsh, D.B., Powell, R.J., Likosky, D.S., and Cronenwett, J.L. (2010). Factors associated with amputation or graft occlusion one year after lower extremity bypass in Northern New England. Ann. Vasc. Surg. *24*, 57–68. https://doi.org/10.1016/j.avsg.2009.06.015.

Hansen, F., Mangell, P., Sonesson, B., and Länne, T. (1995). Diameter and compliance in the human common carotid artery - variations with age and sex. Ultrasound Med. Biol. *21*, 1–9. https://doi.org/10.1016/0301-5629(94)00090-5.

Hiebl, B., Bog, S., Mikut, R., Bauer, C., Gemeinhardt, O., Jung, F., and Krüger, T. (2010). In vivo assessment of tissue compatibility and functionality of a polyimide cuff electrode for recording afferent peripheral nerve signals. Appl. Cardiopulm. Pathophysiol. *14*, 212–219.

Holtby, J.R. (1918). Some indices and measurements of the modern femur. J. Anat. *52*, 363–36382.

Hwang, H.Y., Paeng, J.C., Kang, J., Jang, M.J., and Kim, K.B. (2021). Relation between functional coronary artery stenosis and graft occlusion after coronary artery bypass grafting. J. Thorac. Cardiovasc. Surg. *161*, 1010–1018.e1. https://doi.org/10.1016/j.jtcvs.2020.11.072.

Irimia-Vladu, M. (2014). "Green" electronics: biodegradable and biocompatible materials and devices for sustainable future. Chem. Soc. Rev. *43*, 588–610. https://doi.org/10.1039/c3cs60235d.

Jaspard, F., Nadi, M., and Rouane, A. (2003). Dielectric properties of blood: an investigation of haematocrit dependence. Physiol. Meas. *24*, 137–147. https://doi.org/10.1088/0967-3334/24/1/310.

Khoury, H., Sanaiha, Y., Rudasill, S.E., Mardock, A.L., Sareh, S., and Benharash, P. (2019). Readmissions following isolated coronary artery bypass graft surgery in the United States (from the Nationwide Readmissions Database 2010 to 2014). Am. J. Cardiol. *124*, 205–210. https://doi.org/10.1016/j.amjcard.2019.04.018.

Knappich, C., Kuehnl, A., Haller, B., Salvermoser, M., Algra, A., Becquemin, J., Leo, H., Bulbulia, R., Calvet, D., Fraedrich, G., et al. (2019). Associations of perioperative variables with the 30-day risk of stroke or death in CEA for symptomatic carotid stenosis. Stroke *50*, 3439–3448. https://doi.org/10.1161/STROKEAHA.119.026320.Associations.

Korten, E., Toonder, I.M., Schrama, Y.C., Hop, W.C.J., van der Ham, A.C., and Wittens, C.H.A. (2007). Dialysis fistulae patency and preoperative diameter ultrasound measurements. Eur. J. Vasc. Endovasc. Surg. *33*, 467–471. https://doi.org/10.1016/j.ejvs.2006.10.035.

Lamy, A., Devereaux, P.J., Prabhakaran, D., Taggart, D.P., Hu, S., Straka, Z., Piegas, L.S., Avezum, A., Akar, A.R., Lanas Zanetti, F., et al. (2016). Five-year outcomes after off-pump or on-pump coronary-artery bypass grafting. N. Engl. J. Med. *375*, 2359–2368. https://doi.org/10.1056/nejmoa1601564.

Lane, T.R.A., Metcalfe, M.J., Narayanan, S., and Davies, A.H. (2011). Post-operative surveillance after open peripheral arterial surgery. Eur. J. Vasc. Endovasc. Surg. *42*, 59–77. https://doi.org/10.1016/j.ejvs.2011.03.023.

Leung, W.H., Stadius, M.L., and Alderman, E.L. (1991). Determinants of normal coronary artery dimensions in humans. Circulation *84*, 2294–2306. https://doi.org/10.1161/01.CIR.84.6.2294.

Li, J., Long, Y., Yang, F., Wei, H., Zhang, Z., Wang, Y., Wang, J., Li, C., Carlos, C., Dong, Y., et al. (2020). Multifunctional artificial artery from direct 3D printing with built-in ferroelectricity and tissue-matching modulus for real-time sensing and occlusion monitoring. Adv. Funct. Mater. *30*, 1–10. https://doi.org/10.1002/adfm.202002868.

Lima, F.V., Kolte, D., Kennedy, K.F., Wang, L.J., Abbott, J.D., Soukas, P.A., and Aronow, H.D. (2020). Thirty-day readmissions after carotid artery stenting versus endarterectomy: analysis of the 2013–2014 Nationwide Readmissions Database. Circ. Cardiovasc. Interv. https://doi.org/10.1161/CIRCINTERVENTIONS.119.008508.

Madssen, E., Haere, P., and Wiseth, R. (2006). Radial artery diameter and vasodilatory properties after transradial coronary angiography. Ann. Thorac. Surg. *82*, 1698–1702. https://doi.org/10.1016/j.athoracsur.2006.06.017.

Makin, A., Lip, G.Y.H., Silverman, S., and Beevers, D.G. (2001). Peripheral vascular disease and hypertension: a forgotten association? J. Hum. Hypertens. *15*, 447–454. https://doi.org/10.1038/sj.jhh.1001209.

Mancini, V., Bergersen, A.W., Vierendeels, J., Segers, P., and Valen-Sendstad, K. (2019). High-frequency fluctuations in post-stenotic patient specific carotid stenosis fluid dynamics: a computational fluid dynamics strategy study. Cardiovasc. Eng. Technol. *10*, 277–298. https://doi.org/10.1007/s13239-019-00410-9.

Mannsfeld, S.C.B., Tee, B.C.K., Stoltenberg, R.M., Chen, C.V.H.H., Barman, S., Muir, B.V.O., Sokolov, A.N., Reese, C., and Bao, Z. (2010). Highly sensitive flexible pressure sensors with microstructured rubber dielectric layers. Nat. Mater. *9*, 859–864. https://doi.org/10.1038/nmat2834.

Oda, H., Beker, L., Kaizawa, Y., Franklin, A., Min, J.G., Leyden, J., Wang, Z., Chang, J., Bao, Z., and Fox, P.M. (2020). A novel technology for free flap monitoring: pilot study of a wireless, biodegradable sensor. J. Reconstr. Microsurg. *36*, 182–192. https://doi.org/10.1055/s-0039-1700539.

Ouriel, K. (2001). Peripheral arterial disease. Lancet *358*, 1257–1264. https://doi.org/10.3109/9781420083026.

Pick, J., Stack, J., and Anson, B. (1941). Measurements on the human femur I. Lengths, diamters and angles. Q. Bull. N.U.M.S *15*, 281–290.

Plock, J.A., Schnider, J.T., Schweizer, R., Zhang, W., Tsuji, W., Waldner, M., Solari, M.G., Marra, K.G., Rubin, J.P., and Gorantla, V.S. (2017). The influence of timing and frequency of adipose-derived mesenchymal stem cell therapy on immunomodulation outcomes after vascularized composite allotransplantation. Transplantation *101*, e1–e11. https://doi.org/10.1097/TP.0000000000001498.

Richardson, R.R., Miller, J.A., and Reichert, W.M. (1993). Polyimides as biomaterials: preliminary biocompatibility testing. Biomaterials *14*, 627–635. https://doi.org/10.1016/0142-9612(93)90183-3.

Ruth, S.R.A., and Bao, Z. (2020). Designing tunable capacitive pressure sensors based on material properties and microstructure geometry. ACS Appl. Mater. Interfaces *12*, 58301–58316. https://doi.org/10.1021/acsami.0c19196.

Ruth, S.R.A., Beker, L., Tran, H., Feig, V.R., Matsuhisa, N., and Bao, Z. (2019). Rational design of capacitive pressure sensors based on pyramidal microstructures for specialized monitoring of biosignals. Adv. Funct. Mater. *30*, 1903100. https://doi.org/10.1002/adfm.201903100.

Ruth, S.R.A., Feig, V.R., Kim, M., Khan, Y., Phong, J.K., and Bao, Z. (2020a). Flexible, fringe-effect capacitive sensors with simultaneous high-performance contact and non-contact sensing capabilities. Small Struct. *2*, 2000079. https://doi.org/10.1002/sstr.202000079.

Ruth, S.R.A., Feig, V.R., Tran, H., and Bao, Z. (2020b). Microengineering pressure sensor active layers for improved performance. Adv. Funct. Mater. *30*, 2003491. https://doi.org/10.1002/adfm.202003491.

Sandgren, T., Sonesson, B., and Ahlgren, Å.R. (1998). Factors predicting the diameter of the popliteal artery in healthy humans. J. Vasc. Surg. *28*, 284–289.

Schneider, F., Fellner, T., Wilde, J., and Wallrabe, U. (2008). Mechanical properties of silicones for MEMS. J. Micromech. Microeng. *18*, 065008. https://doi.org/10.1088/0960-1317/18/6/065008.

Spector, K.S., and Laweson, W.E. (2001). Optimizing safe femoral access during cardiac catheterization. Catheter Cardiovasc. Interv. *53*, 209–212.

Stroke (2017). Centers for Disease Control and Prevention. cdc.gov.

Sun, Y., Lacour, S.P., Brooks, R.A., Rushton, N., Fawcett, J., and Cameron, R.E. (2009). Assessment of the biocompatibility of photosensitive polyimide for implantable medical device use. J. Biomed. Mater. Res. A *90*, 648–655. https://doi.org/10.1002/jbm.a.32125.

Swartz, W.M., Jones, N.F., Cherup, L., and Klein, A. (1988). Direct monitoring of microvascular anastomoses. Plast. Reconstr. Surg. *81*, 149–158.

Tu, J.V., Wang, H., Bowyer, B., Green, L., Fang, J., and Kucey, D. (2003). Risk factors for death or stroke after carotid endarterectomy: observations from the Ontario Carotid Endarterectomy Registry. Stroke *34*, 2568–2573. https://doi.org/10.1161/01.STR.0000092491.45227.0F.

Vardoulis, O., Saponas, T.S., Morris, D., Villar, N., Smith, G., Patel, S., and Tan, D. (2016). In vivo evaluation of a novel, wrist-mounted arterial pressure sensing device versus the traditional hand-held tonometer. Med. Eng. Phys. *38*, 1063–1069. https://doi.org/10.1016/j.medengphy.2016.06.022.

Victor, A., Ribeiro, J.F., and Araújo, F. (2019). Study of PDMS characterization and its applications in biomedicine: a review. J. Mech. Eng. Biomech. *4*, 1–9. https://doi.org/10.24243/jmeb/4.1.163.

Virani, S.S., Alonso, A., Benjamin, E.J., Bittencourt, M.S., Callaway, C.W., Carson, A.P., Chamberlain, A.M., Chang, A.R., Cheng, S., Delling, F.N., et al. (2020). Heart disease and stroke statistics—2020 update: a report from the American Heart Association. Circulation. https://doi.org/10.1161/CIR.0000000000000757.

Widodo, C.S., Sela, H., and Santosa, D.R. (2018). The effect of NaCl concentration on the ionic NaCl solutions electrical impedance value using electrochemical impedance spectroscopy methods. In AIP Conference Proceedings, p. 050003. https://doi.org/10.1063/1.5062753.

Zipper, J.A., Tatum, H.J., Pastene, L., Medel, M., and Rivera, M. (1969). Metallic copper as an intrauterine contraceptive adjunct to the "T" device. Am. J. Obstet. Gynecol. *105*, 1274–1278. https://doi.org/10.1016/0002-9378(69)90302-0.

STAR★METHODS

KEY RESOURCES TABLE

REAGENT or RESOURCE	SOURCE	IDENTIFIER
Chemicals, peptides, and recombinant proteins		
Sylgard 184	DOW Corning USA	Material Number 1024001
trichloro(1H,1H,2H,2H-perfluorooctyl)silane	Sigma-Aldrich	CAS Number: 78560-45-9
Sil-Poxy	Smooth-On	https://www.smooth-on.com/products/sil-poxy/
paraformaldehyde	Sigma-Aldrich	CAS Number: 30525-89-4
Experimental models: Organisms/strains		
Sprague Dawley Rats	ENVIGO	https://www.envigo.com/
Software and algorithms		
MATLAB 2013	MathWorks	https://www.mathworks.com/products/matlab.html
Origin 2021	OriginLab	https://www.originlab.com/2021
Other		
Agilent E4980A Precision LCR meter	Agilent	Model number: E4980A
Texas Instruments FDC1004EVM-4 Channel Capacitive to Digital Converter Evaluation Module	Texas Instruments	https://www.ti.com/tool/FDC1004EVM
Lynxmotion Little Grip Kit	Robotshop	Lynxmotion.com
Arduino Uno, Rev 3	Arduino	Code: A000066
Central Line Pump	Syndaver	SKU: 160503
Platform Pump	Syndaver	SKU: 170130
Cook-Swartz Doppler Probe	Cook Medical	Reference Part Number: DP-SDP001

RESOURCE AVAILABILITY

Lead contact

Further information and requests for resources and reagents should be directed to and will be fulfilled by the lead contact, Zhenan Bao (zbao@stanford.edu).

Materials availability

This study did not generate new unique reagents.

Data and code availability

All data reported in this paper will be shared by the lead contact upon request. This paper does not report original code.

EXPERIMENTAL MODEL AND SUBJECT DETAILS

In vivo animal models

Sensor function assessment. Ten healthy Sprague Dawley (SD) rats (12-20 weeks, 300–350 g, male, Envigo) were used in compliance with the regulations of animal care and use committee of our hospital. Each rat was single-housed after the initial surgery.

Biocompatibility testing. Eighteen healthy SD rats (11-13 weeks, 300-360g, mean 333.6g male, ENVIGO) were used in compliance with the regulations of Institutional Animal Care and Use Committee (IACUC). Each rat was single-housed after the initial surgery.

METHOD DETAILS

Silicon mold fabrication

The molds used to make the pyramid microstructures was made by patterning bare <100> Si wafers with a 300 nm thermally grown oxide. The process starts with a lithography process to generate photoresist patterns (S1813, Microposit) and etching of the oxide layer using buffered oxide etch (6:1, BOE) for 45 minutes. Then, the remaining oxide layer acts as a mask during the Si etching process. By using KOH (30% at 80C) <100> Si can be etched to create pyramid structures with a sidewall angle of 54.7. The oxide layer is subsequently removed using buffered hydrofluoric acid, followed by a vapor deposition of trichloro(1H,1H,2H,2H-perfluorooctyl)silane (Sigma-Aldrich) for ease of release from the mold. In this case, the pyramid microstructure base itself was 50 μm × 50 μm with 50 μm separation between the structures.

Microstructure fabrication

A 23:1 Sylgard 184 (polydimethyl siloxane (PDMS)) from DOW Corning USA) elastomer to crosslinker ratio was mixed using FlackTek, Inc. speedmixer at 2500 rpm for 5 minutes followed by at least a 10 minute degas by vacuum. Once finished, the mixture (600 μL) was transferred on to cover the entire the silicon wafer mold (1.5 x 1.5 cm^2) and spin coated at 500 rpm (100 rpm/s acceleration) for 1 minute. Finally, it was degassed by vacuum for 1 hour, cured at 70°C for 2 days, and demolded.

Encapsulation layer fabrication

A 10:1 Sylgard 184 elastomer to crosslinker ratio was mixed using FlackTek, Inc. speedmixer at 2500 rpm for 5 minutes followed by at least a 10 minute degas by vacuum. Once finished, the mixture (1500 μL) was transferred on to cover the entire the silicon wafer (1/4 of 8'' silicon wafer) previously treated with trichloro(1H,1H,2H,2H-perfluorooctyl)silane (Sigma-Aldrich) and spin coated at 500 rpm (100 rpm/s acceleration) for 90 seconds. Finally, it was degassed by vacuum for 2 hours and cure at 70°C for 18 hours, and demolded.

Sensor assembly

The electrodes were designed and purchased from PCBWay. The polyimide layer is 80 μm (wireless) or 100 μm (wired) thick with 18 μm thick copper on top. The electrode is placed on the thin PDMS encapsulation layer. The pyramid microstructures were placed on the electrodes with the tips facing the electrodes. A thin layer of Sil-Poxy (Smooth-On) was deposited around the outside of the polyimide on the lower encapsulation layer. The upper encapsulation layer was then placed on top with air bubbles removed.

Normal force testing

The Agilent E4980A Precision LCR meter was used to take the capacitance measurements at 15 kHz frequency with a 5 V a.c. signal. A force gauge (Mark-10, Series 5, Force Gauge Model M5-10) along with a mechanized z-axis stage were used to apply the pressures to the sensors. Measurements were performed at controlled temperature (23.5 ± 1°C) and humidity (40 ± 10%). 5 cycles with a step size of 2 μm to a maximum for of 0.5 N and 10 N were repeated for all sensors.

In vitro testing – Air pump

These studies were conducted using Texas Instruments FDC1004EVM- 4 Channel Capacitive to Digital Converter Evaluation Module. Measurements were taken at a sampling frequency of 400 samples per second. For the pulsation response testing, air is pumped using an air pump (Philips Avent Electric Breast Pump SCF312/01) into a polyolefin tube with 5- or 6-mm inner diameter. Sensors were evaluated at three pumping rates—45, 60, and 80 bpm— to mimic a range of arterial pulse rates. To mimic the *in vivo* environment, 1-lb of 10-cm x 10-cm artificial fat, skin, and muscle was applied to the sensor wrapped around the polyolefin tube (Syndaver).

In vitro testing - Syndaver

The wired sensor studies were performed using Texas Instruments FDC1004EVM - 4 Channel Capacitive to Digital Converter Evaluation Module. Measurements were taken at a sampling frequency of 400 samples per second. For the response to different artificial arteries—2 mm, 4 mm, 6 mm, and 7 mm in diameter (Syndaver, USA)—a continuous steady flow platform pump (Syndaver) was used together with artificial skin, fat, and muscle (Syndaver) to mimic the *in vivo* environment of the vessels. Blockages were introduced via stenosis of the vessel at 1 mm diameter increments with a 0.5-mm rubber tube. Sensor response was

measured from distances 0-10 cm both upstream and downstream of the stenosis. Pulsations were introduced using a Lynxmotion Little Grip Kit (Robotshop) robotic gripper. The robot gripper was connected to a microcontroller (Arduino Uno, Rev 3) with a feedback loop developed using the microcontroller's software. The gripper was set to fluctuate between 5 and 6 mm at a rate of 60 cycles per second. The gripper was placed 4-5 cm upstream of the sensor and stenoses were introduced between the gripper and the sensor.

Wireless testing

Testing is performed using a Mini Vector network Analyzer (VNA) Tiny Plus (mini-VNA, Xuanli Electronic Technology Factory, China). Pressure response curves are generated by applying weights 1-100g on the sensor and measuring the frequency change. *In vitro* performance is confirmed using the Syndaver *in vitro* setup with a 1-2 mm thick artificial skin layer (Syndaver) added between the sensor antenna and the reader coil.

Cadaver model

A fresh cadaver (age 77) was obtained through the University of California San Francisco (UCSF) Willed Body Program according to the standard operating procedures of Stanford University Anatomy Lab. At room temperature, the common and superficial femoral arteries were exposed. Standard polyvinyl chloride (PVC) tubing with a $^1/_4$" barbed lightweight quick-turn tube coupling (McMaster-Carr) was used to connect the artery to the central line pump (Syndaver) with pulsatile blood flow into the artery and drainage blood flow out of the artery. 0.15-0.2 mol/L sodium chloride in deionized water was pumped through the artery. The sensor was wrapped around the femoral artery and fixed with a surgical clamp on each side. Occlusions were introduced both upstream and downstream of the sensor using a surgical tie. Sensor response was evaluated at 60 bpm.

In vivo testing – Sensor function assessment

The implantation surgery was performed under isoflurane inhalation anesthesia with bupivacaine (Hospira) for local anesthesia. Slow-release buprenorphine (ZooPharm) was administered as pain medication once prior to surgery. Rats were anesthetized with 2-3% isoflurane. All sensors were sterilized using iodine and ethanol prior to implantation. The sensor was wrapped around the femoral vessel and fixed to with sutures. For wireless sensor testing, the coil structure of the device was placed directly beneath the skin in a skin pocket surgically created. Each animal was administered Enrofloxacin (Enroflox) for antibiotic prophylaxis prior to the surgery and for three days following the surgery. Temporary (<30 seconds) partial occlusions were introduced using microsurgical clips. The rats were monitored for three weeks. At the conclusion of the study, the animals were euthanized humanely, and samples were harvested for biocompatibility evaluation. This study was repeated to confirm results with four additional SD rats, with adjustments made to the overall length of PDMS encapsulation layer (addition of ~5 mm) and fixation of the sensor with microclips (Teleflex, USA). During the course of the second study, one of the rats was euthanized due to an unrelated illness. The same procedure was also repeated with the Cook-Swartz Doppler Probe (Cook Medical, USA) wrapped around the femoral artery (n=2) and secured with microclips (Teleflex). All procedures were approved by the institutional review board and the animal care and use committee at the Veterans Affairs Palo Alto.

Biocompatibility – Surgery

The biocompatibility of PDMS and polyimide were histologically evaluated and compared with poly(octamethylene maleate (anhydride) citrate (POMaC)—a biodegradable material—and a sham. Eighteen SD rats (11-13 weeks, 300-360g, mean 333.6g male, ENVIGO) were used in compliance with the regulations of Institutional Animal Care and Use Committee (IACUC). SD rats were housed in a 12/12-hour light/dark cycle and given food and water. Nine rats were euthanized at one week and 7 rats were euthanized at 12 weeks after the implantation for testing of biocompatibility to have three samples of each material at each time points. Two rats were euthanized due to animal welfare protocols. Rats were anesthetized using 2-3% isoflurane. Animals were given Baytril (5 mg/kg) and Buprenorphine (0.05 mg/kg) injections before skin incision. After the material was disinfected with iodine, the material was wrapped around the femoral artery and secured. After implantation, the wound was closed with 5-0 Nylon suture. On the contralateral hind limb, we performed a sham operation or implanted the same material sheet using the same anterior approach to expose the femoral artery and vein from the inguinal ligament to the bifurcation of the deep

femoral vessels. After the sham operation or material implanting, the wound was closed with 5-0 Nylon suture. Following surgery, Buprenorphine was administered as postoperative analgesia every 12 hours for 3 days along with Baytril.

Biocompatibility – Tissue harvest and assessment

The femoral artery and remnants of the materials were harvested from the femoral artery and samples were fixed with 4% paraformaldehyde in 0.1 M phosphate buffer (pH 7.4) overnight at 4°C. 25 μm thick transverse sequential frozen sections were prepared and then some were stained with hematoxylin and eosin. Samples were analyzed using a Keyence BZ-X700 microscope (Japan). The diameter of the arterial lumen and the intima thickness ratio of the femoral artery were measured. Based on previous work, the intima thickness ratio was defined as [intima thickness / (intima thickness + media thickness)] x 100 (Plock et al., 2017).

For rats monitored for *in vivo* testing with the entire sensor (n=3), part of the femoral artery the sensor was wrapped around was harvested with surrounding soft tissue. As a control, the femoral artery that did not have the wireless sensor wrapped around was harvested as well. Tissue assessment was repeated on these samples, as described above.

QUANTIFICATION AND STATISTICAL ANALYSIS

Statistical analysis

To compare the biocompatibility among the material groups and the sham control group at each time point, a one-way ANOVA was performed, followed by a Tukey-Kramer honestly significant difference (HSD) test as a post hoc test. To compare the biocompatibility between two time points in each the material group or sham control group, a student's t-test was performed. The results from sensor biocompatibility are presented as mean and standard deviation. Differences were considered significant at $p < 0.05$.